Rare Metal Materials and Engineering
Volume 55, Issue 9, September 2026
Available online at www.rmme.ac.cn

Science Press

Cite this article as: Luo Fenglin, He Quanfeng, Wang Xufeng, et al. Effect of Al/Ti Ratio on Phase Stability and Mechanical Properties of Ti-Al-Based Lightweight High-Entropy Alloys[J]. Rare Metal Materials and Engineering, 2026, 55(09): 2117-2132. DOI: https://doi.org/10.12442/j.issn.1002-185X.20250510.

ARTICLE

Effect of Al/Ti Ratio on Phase Stability and Mechanical Properties of Ti-Al-Based Lightweight High-Entropy Alloys

Luo Fenglin[1,2], He Quanfeng[2], Wang Xufeng[2], Zhang Yi[2], Wang Yiwei[2], Kuang Xiangyi[1,2], Gu Jianfeng[2], Wang Qing[1]

[1] Institute of Materials, Shanghai University, Shanghai 200072, China; [2] Institute of Materials Modification & Modelling, School of Materials Science and Engineering, Shanghai Jiao Tong University, Shanghai 200240, China

Abstract: Lightweight high-entropy alloys (LWHEAs) represent a promising class of materials for advanced structural applications. However, achieving precise control over their phase formation and mechanical properties remains a significant challenge. Although the conventional empirical parameters (mixing enthalpy ΔH_{mix}, valence electron concentration, atomic size mismatch δ, and electronegativity difference Φ) provide general guidance for phase stability in Ti-Al-based LWHEAs, their predictive accuracy is restricted. The Al/Ti atomic ratio (γ, namely Al/Ti ratio) is a more decisive and precise criterion for microstructure control. Guided by this parameter, a series of $Ti_{(50-x)}Al_{(6.5+x)}V_{11.5}Nb_{14.5}Zr_{17.5}$ alloys were designed and synthesized. Results reveal that γ critically governs the precipitation, extent of short-range ordering, and grain refinement of B2 phase. Additionally, a moderate γ value of approximately 2.0 ($Ti_{46}Al_{10.5}$ alloy) yields an optimal synergy of high yield strength (>1 GPa) and considerable tensile ductility (>20%), whereas excessively high γ leads to embrittlement. This work considers γ as a key compositional parameter and provides a practical framework for designing high-performance LWHEAs through integrated parametric and element-ratio control.

Key words: LWHEAs; empirical parameters; Al/Ti ratio; B2 phase; short-range ordering; microstructure; mechanical properties

1 Introduction

Lightweight alloys are extensively employed in the structural design of aerospace, aviation, and automotive applications, where reducing energy consumption and minimizing environmental impact are primary goals. Conventional lightweight alloy systems, based mainly on aluminum, magnesium, and titanium, face several restrictions, including inadequate room-temperature strength and ductility[1], inferior corrosion resistance[2], difficult processing[3], and inherent inability to achieve a satisfactory balance between room-temperature toughness and high-temperature performance[4]. These shortcomings significantly restrict their broader application. In recent years, lightweight high-entropy alloy (LWHEA) has emerged as a promising alternative. Based on the multi-principal-element systems without a single dominant component[5], LWHEAs benefit from unique thermodynamic and kinetic effects that lead to distinctive structural characteristics, which expands the compositional space for microstructure tailoring, enabling more precise control over the phase stability and mechanical properties. Consequently, LWHEAs offer a viable pathway to overcome the problems of conventional lightweight alloys.

LWHEAs mainly have body-centered cubic (bcc) structures[6]. To enhance the mechanical properties of LWHEAs, considerable research attention has recently been directed toward the formation of chemically ordered B2 phases and nanoscale precipitates within bcc matrices[6]. Current studies focus mainly on compositional adjustments, such as varying the concentrations of Ti, Al, and Nb[7–8], or adding elements Zr and Cr, to modulate phase stability and ordering tendencies[9–11]. Besides, thermomechanical processing routes,

Received date: September 30, 2025
Foundation item: National Natural Science Foundation of China (52301211)
Corresponding author: He Quanfeng, Ph. D., Institute of Materials Modification & Modelling, School of Materials Science and Engineering, Shanghai Jiao Tong University, Shanghai 200240, P. R. China, E-mail: hequanfeng@sjtu.edu.cn; Gu Jianfeng, Ph. D., Institute of Materials Modification & Modelling, School of Materials Science and Engineering, Shanghai Jiao Tong University, Shanghai 200240, P. R. China, E-mail: gujf@sjtu.edu.cn; Wang Qing, Ph. D., Institute of Materials, Shanghai University, Shanghai 200072, P. R. China, E-mail: qingwang@shu.edu.cn

including heat treatment[12] and rolling followed by annealing[13], have been used to control microstructure and defect formation. Increasingly, integrated approaches combining composition design with processing strategies have been adopted for synergistic microstructure optimization[14].

Notably, the Al and Ti are identified as critical factors influencing the phase formation and stability in Ti-Zr-Al-Nb-V-based LWHEAs[7]. For instance, Stepanov et al[8] investigated the $Al_xNbTiVZr$ system and observed that increasing Al content promoted the formation and morphology evolution of Laves phases, significantly altering the microstructure and properties. Similarly, Klimenko et al[15] reported that higher Al content led to multiphase structures containing bcc, Laves, and Zr-Al intermetallic compounds. Wang et al[7] further demonstrated that adjusting Ti and Al contents could effectively suppress the formation of B2 and Laves phases, underscoring the importance of Ti-Al interactions in regulating the phase stability. In alignment with trends in conventional alloy design, research on LWHEAs has evolved from pursuing single-phase solid solutions toward dual- or multiphase structures to achieve superior mechanical performance[6]. Most LWHEA systems are based on Ti with additions of Al, Nb, V, and Zr. For better balance among strength, high-temperature stability, and ductility, specific strategies (alloying with Cr, Mo, or Y[16–17], adjusting the base element ratios, and applying the thermomechanical process) have been employed[7,13]. These methods promote the formation of nanoscale B2 precipitates or ordered clusters within the bcc matrix, effectively improving the strength without severe loss of ductility. For example, Zherebtsov et al[13] reported that cold rolling and annealing for $Al_5Nb_{24}Ti_{40}V_5Zr_{26}$ alloy resulted in a good combination of strength and ductility after recrystallization. Conversely, Wang et al[18] showed that aging treatment for $Ti_{50}Zr_{18}Nb_{15}V_{12}Al_5$ alloy promoted the ordering similar to B2 phase, which enhanced work-hardening behavior and resulted in high uniform elongation alongside high strength. Similarly, Lv et al[19] used rapid solidification to refine microstructure and introduce secondary phase particles, achieving simultaneous improvements in strength and ductility.

Despite these advances, the fundamental challenge of achieving an optimal balance among high ductility at room temperature, high-temperature strength, and long-term thermal stability remains unresolved. This challenge stems primarily from the insufficient understanding of the factors governing the formation of ordered B2 phases, the stability of secondary intermetallic compounds, and their collective influence on deformation mechanisms. In this study, the effect of Al/Ti ratios on the phase evolution, micromechanical behavior, and tensile properties of TiZrAlNbV-based LWHEA was investigated. Through the combination of advanced theoretical analysis and mechanical tests, the microstructure-property relationships were established, thereby providing crucial insights for the design of next-generation lightweight structural alloys with enhanced mechanical properties.

2 Design Strategies for LWHEAs

Based on the empirical criteria and thermodynamic principles, the relationships among key thermodynamic parameters—mixing enthalpy (ΔH_{mix}), valence electron concentration (VEC), atomic size mismatch (δ), and electronegativity difference (Φ) —were investigated. Graphical analyses were used to identify the characteristic parameter ranges related to the coexistence of B2 phases and improved tensile ductility, thereby establishing useful alloy design principles. Empirical rule was also proposed: the Al/Ti ratio in Ti-Al-based systems was a useful indicator for the formation of ordered B2 phases.

2.1 Criteria for phase selection and prediction in LWHEAs

2.1.1 Traditional empirical parameters

Unlike conventional alloys based on one or two principal elements, the high-entropy alloys are characterized by their distinctive thermodynamic high-entropy effect[20], which suppresses the formation of multiple competing intermetallic compounds and promotes the stabilization of single-phase solid solutions. Basically, the thermodynamic criteria used to describe phase selection and stability in high-entropy alloys are extensions of the classical Hume-Rothery rules. Commonly employed empirical thermodynamic descriptors include ΔH_{mix}, mixing entropy (ΔS_{mix}), δ, electronegativity difference ($\Delta\chi$), and VEC[21–24]. For instance, Zhang et al[21] proposed the δ - ΔH_{mix} relationship to predict phases and assess phase stability in multi-principal element alloys, and rationalized the phase formation trends in systems, such as AlTiVYZr and ZrTiVCuNiBe. Thus, the parameter Ω was introduced as an additional thermodynamic descriptor, suggesting that higher Ω values generally favor single-phase solid solutions, while lower Ω values tend to promote multiphase formation[23]. To further improve the predictive accuracy, Senkov et al[25] proposed the parameter Φ to guide the design of high-entropy alloys, which provides clearer phase boundaries than earlier criteria, as shown in Fig.1a. Similarly, Guo et al[24] highlighted the decisive role of VEC in structural stability: face-centered cubic (fcc) phases are typically stabilized at VEC≥8, bcc phases are typically stabilized at VEC<6.87, and intermediate values (6.87≤VEC<8) often lead to mixed bcc+fcc microstructures. Therefore, these parameters, whether considered individually or in combination, serve as valuable empirical guidelines for evaluating the possibility of solid-solution versus multiphase formation. Although inherently simplified, they have proven effective for rapid screening and preliminary design of high-entropy alloy systems.

Due to these advances, empirical design frameworks, such as δ - ΔH_{mix}, δ - Φ, and Φ -VEC, have been widely applied to guide phase selection and prediction of high-entropy alloys[23,26–32]. It should be noted that these criteria have only been developed and validated primarily for equiatomic or near-equiatomic systems, whereas their applicability to LWHEAs remains obscure. Owing to the distinct thermodynamic characteristics of LWHEAs, including strong

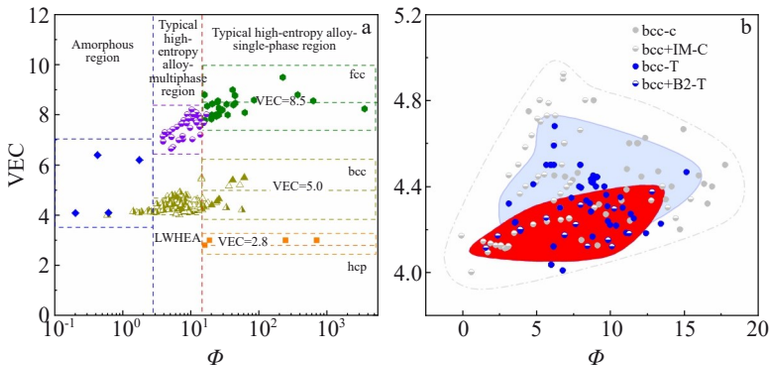

Fig.1 Relationships of Φ-VEC of various alloys: (a) typical high-entropy alloys and LWHEAs materials; (b) magnified view of LWHEA-related region

enthalpic interactions and the tendency for short-range ordering (SRO), the direct transferability of conventional design rules cannot be assumed.

Fig. 1a presents a systematic analysis of the relationship between the structural parameter Φ and VEC for representative high-entropy alloys, LWHEAs, and amorphous alloys. Symbols C and T represent compressive and tensile plasticity, respectively; IM indicates the intermetallic phase; hcp indicates the close-packed hexagonal structure. More detailed data are listed in Table S1 and Table S2 in the Supplement. The tensile and compressive mechanical properties are compared, particularly the stress σ and strain ε. For LWHEAs, the Φ-VEC distributions are confined to a relatively narrow compositional domain, i.e., VEC values are typically in the range of 4–5, whereas Φ has a broader range. Fig.1b further illustrates the Φ-VEC correlation for LWHEAs. LWHEAs exhibiting compressive plasticity occupy a broad Φ-VEC domain that largely encompasses the composition space of alloys with great tensile plasticity. Within this parameter space, however, the multiphase and single-phase alloys do not exhibit well-defined phase boundaries. Notably, alloys containing B2 phase generally show relatively low Φ and VEC values, underscoring the critical influence of these two parameters on the phase constitution and mechanical behavior. Interestingly, alloys located within the nominal single-phase bcc or amorphous regions in the Φ-VEC diagram frequently develop persistent multiphase microstructures in practice. This discrepancy highlights the limited predictive accuracy of phase selection based solely on a two-dimensional Φ-VEC correlation in LWHEAs. Nonetheless, the proposed guideline offers a practical parameter window for tailoring the microstructural stability of bcc+B2 alloys.

In LWHEAs, the parameter δ plays a critical role in governing lattice distortion, phase stability, phase separation, local chemical ordering, and precipitate formation[33]. Fig. 2 illustrates the relationship between δ and Φ and its influence on phase constitution. Feng et al[22] reported that when Φ<20, high-entropy alloys tend to form multiphase structures. As shown in Fig. 2, the Φ values of LWHEAs are mostly below 17, within which both single-phase and multiphase structures can be observed. Because LWHEAs lack tensile plasticity, a

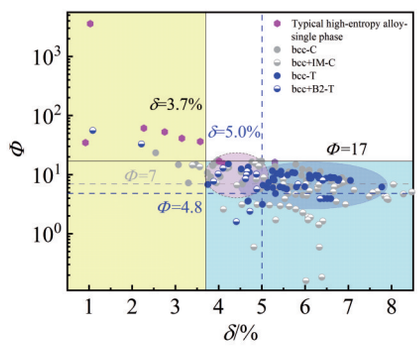

Fig.2 Relationship of Φ with δ for typical high-entropy alloys and LWHEAs

threshold of $\Phi\approx7$ can effectively distinguish the single-phase and multiphase alloys. By contrast, alloys exhibiting tensile plasticity display a narrower distribution of Φ values without a sharp boundary. Notably, multiphase alloys containing B2 phase generally correspond to relatively small δ values. Neglecting the kinetic effects, phase formation is thermodynamically governed by the Gibbs free energy, which is strongly influenced by the ΔH_{mix} [34]. The magnitude and sign of ΔH_{mix} directly reflect the nature of atomic interactions. A positive ΔH_{mix} promotes atomic segregation, favoring phase separation or amorphous formation. When ΔH_{mix} is near zero, atomic interactions are weak, allowing configurational entropy to dominate and thereby stabilizing the single-phase solid solutions. Conversely, a strongly negative ΔH_{mix} indicates strong metallic or covalent bonding, which promotes ordered intermetallic compounds or local chemical SRO[35].

In bcc-structured LWHEAs, the influence of strongly negative mixing enthalpy on secondary-phase precipitation is decisive, dominant, and often rapid. Its impact is more pronounced and direct in bcc systems than in fcc ones, owing to the synergistic interaction between the intrinsic characteristics of the bcc lattice and the thermodynamic driving force associated with highly negative mixing enthalpy.

The ordered B2 phase serves as the most representative example. In this structure, one atomic species preferentially occupies the body-centered sites, while the other occupies the corner sites, forming a long-range ordered arrangement.

Element pairs with strongly negative mixing enthalpy (Al-Ni, Al-Zr, and Al-Ti) spontaneously develop the ordering tendencies. As a result, in many Al- or Ti-containing bcc high-entropy alloys[11], such as AlCoCrFeNi and TiZrNbAl systems, the B2 phase often coexists with the disordered bcc matrix, even in the as-cast condition, appearing in eutectic or dendritic morphologies without the need for additional thermal treatments to induce precipitation.

When ΔH_{mix} becomes excessively negative, the system may undergo amorphization. This tendency is closely associated with the large atomic size mismatch, which destabilizes the crystalline lattice, induces local collapse, and thereby favors amorphous phase formation[36]. The interplay between ΔH_{mix} and δ thus serves as a critical criterion for phase selection and structural prediction in high-entropy alloys. As shown in Fig. 3, LWHEAs are generally located within the transition region between single-phase and multiphase regimes in the ΔH_{mix}-δ parameter space, spanning a relatively broad range of values. The combination of a decrease in ΔH_{mix} and an increase in δ strengthens the driving force for atomic ordering[21], thereby facilitating the transformation from single-phase bcc solid solutions to multiphase bcc+B2 ones.

2.1.2 Al/Ti ratio as a determinant of B2 phase formation

Although existing parametric criteria provide general guidance for predicting multiphase formation, their effectiveness is often limited by broad parameter ranges and poorly defined phase boundaries. Recent studies on the Ti-Al-Nb-V-Zr alloy system have demonstrated that element Al is both necessary and sufficient for stabilizing the B2 phase, whereas Ti is indispensable for maintaining the bcc matrix[37]. The critical role of Al and Ti can be rationalized through their influence on fundamental thermodynamic and electronic parameters. Increasing Al concentration reduces the VEC value and drives

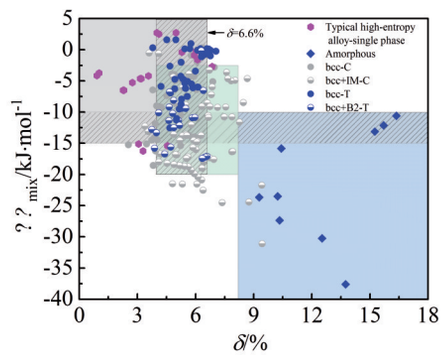

Fig.3 Relationship between ΔH_{mix} and δ of amorphous materials, typical high-entropy alloys, and LWHEAs

ΔH_{mix} toward more negative values, both of which strengthen the ordering tendency and promote B2 formation. In contrast, Ti stabilizes the disordered bcc solid solution and alleviates excessive lattice distortion, thereby suppressing the formation of brittle intermetallic compounds. Consequently, the Al/Ti ratio emerges as a decisive compositional parameter governing the balance between ordered B2 domains and disordered bcc regions. A systematic evaluation of both the absolute concentrations of Al and Ti and their ratio is therefore essential for the rational design of LWHEAs with tailored microstructures, optimized strength-ductility synergy, and reliable high-temperature performance. Based on these findings, a specific atomic percentage ratio of Al to Ti (γ) is defined as a key parameter for the phase selection in LWHEAs, as follows:

$$\gamma = \frac{C_{Al}}{C_{Ti}} \times 10 \quad (1)$$

where C_{Al} and C_{Ti} are concentrations of elements Al and Ti, respectively.

As illustrated in Fig. 4, a critical threshold of γ =1.87

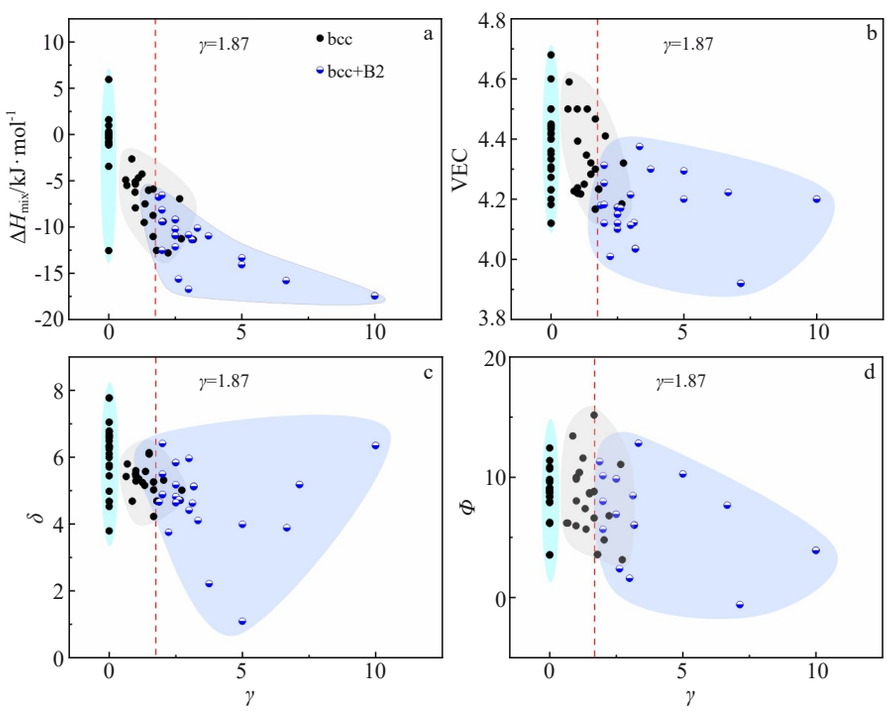

Fig.4 Relationships of ΔH_{mix}-γ (a), VEC-γ (b), δ-γ (c), and Φ-γ (d)

effectively delineates the boundary between single-phase bcc and bcc+B2 multiphase alloys. Alloys with γ<1.87 predominantly form single-phase bcc structures, whereas those with γ> 1.87 consistently develop bcc+B2 multiphase microstructures. This transition can be rationalized by considering both thermodynamic and electronic effects: aluminum, with its relatively low VEC value of 4, reduces the overall VEC value of the alloy as its content increases. Simultaneously, the strongly negative ΔH_{mix} values of binary Al-Nb and Al-Ti systems drive the overall ΔH_{mix} toward more negative values with the increase in γ value, thereby enhancing the stability of B2 phase.

A reduced VEC favors the stabilization of disordered bcc solid solutions, while increasingly negative ΔH_{mix} promotes short-range chemical ordering and nano-precipitation. In the alloys exhibiting tensile ductility, the combined influence of these factors enhances the tendency for B2 phase formation. Accordingly, with the increase in γ, the governing parameters (VEC, ΔH_{mix}, δ, and Φ) all exhibit a general decreasing trend, which synergistically drives the structural transition and defines a clear compositional boundary. Thus, γ can be regarded as a decisive compositional variable to design the bcc+B2 multiphase structures. This γ-based criterion not only provides a physically grounded explanation for ordered phase formation but also serves as a practical guideline for optimizing the mechanical performance of LWHEAs through composition design.

Fig. 5 summarizes the relationship between γ and the microstructural evaluation in LWHEAs exhibiting only compressive plasticity. The formation of secondary phases in alloys without tensile ductility is not strictly governed by γ with values spanning a broad range (γ=0–20). These systems typically contain a variety of complex intermetallic precipitates, including B2 phase, Laves phase, and other Zr-Al phases. In contrast, Fig. 6 illustrates the correlation between crystal structure and γ value of LWHEAs exhibiting tensile ductility. In these alloys, precipitates are predominantly B2-structured, and the overall phase constitution is considerably simpler than that in alloys lacking tensile plasticity. This is mainly because other ordered phases often have a devastating impact on tensile plasticity. For example, when TiZrAlNbV undergoes aging, an Omega phase rich in Zr and Al is precipitated, and the plasticity of the alloy drops sharply from above 25% to about 2%[14]. Therefore, in current research, alloys with tensile plasticity often have bcc/B2 structures. A distinct structural transition occurs at γ≥1.87, above which the B2 phase typically appears. It should be noted that a few alloys remain in a single-phase bcc state, even when γ exceeds this threshold.

These observations indicate that although γ serves as a valuable guideline for predicting the propensity for B2 formation, it is not the sole determinant of phase stability. The absolute concentrations of Al and Ti also critically influence phase constitution. Therefore, the rational design of LWHEAs with tensile ductility requires consideration of both the γ value and the individual elemental concentration to achieve targeted microstructures and optimized mechanical properties. Importantly, compared with the relatively broad and overlapping ranges defined by δ-ΔH_{mix} or Φ-VEC criteria, the γ parameter provides a more restrictive and practically actionable boundary, offering a sharper compositional design tool for tailoring LWHEAs.

2.2 Mechanical property screening based on empirical parameters

To screen out LWHEAs with superior mechanical properties and tensile ductility, the possible correlation among the

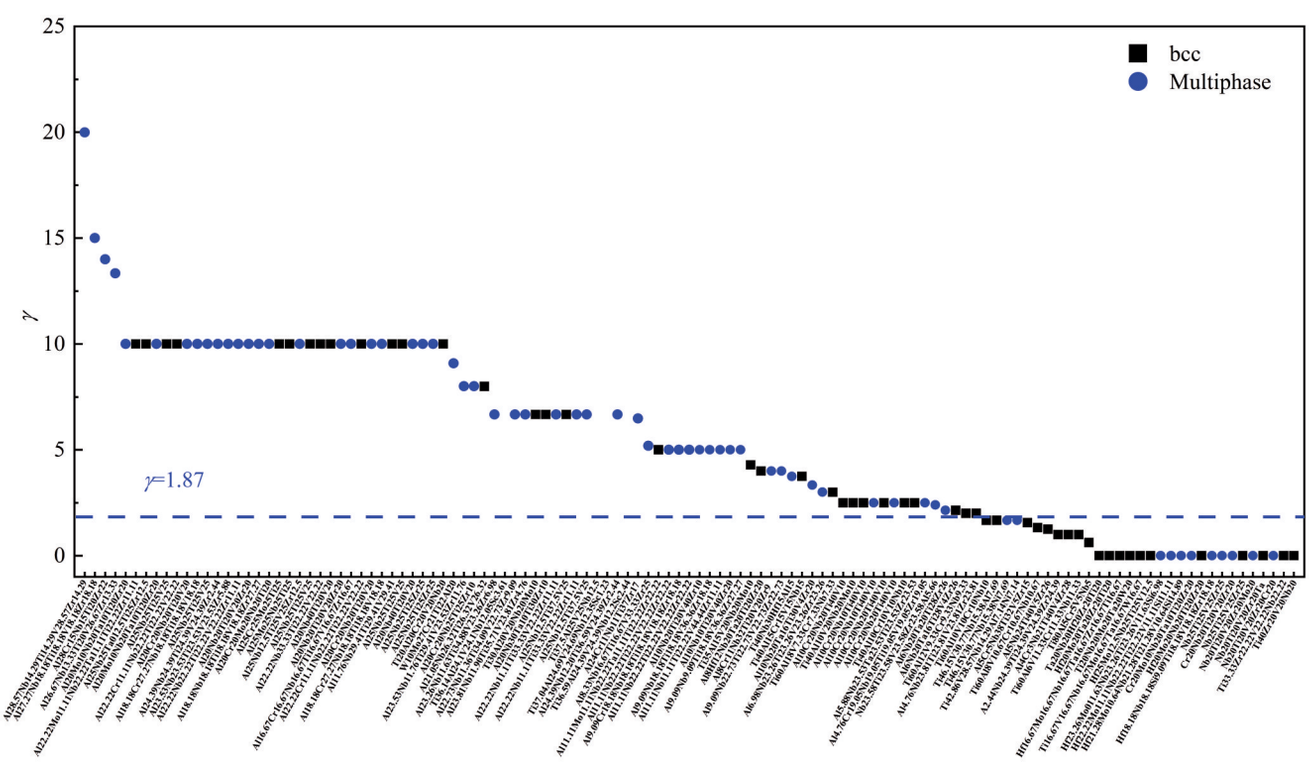

Fig.5 Phase constitution of LWHEAs exhibiting compressive plasticity

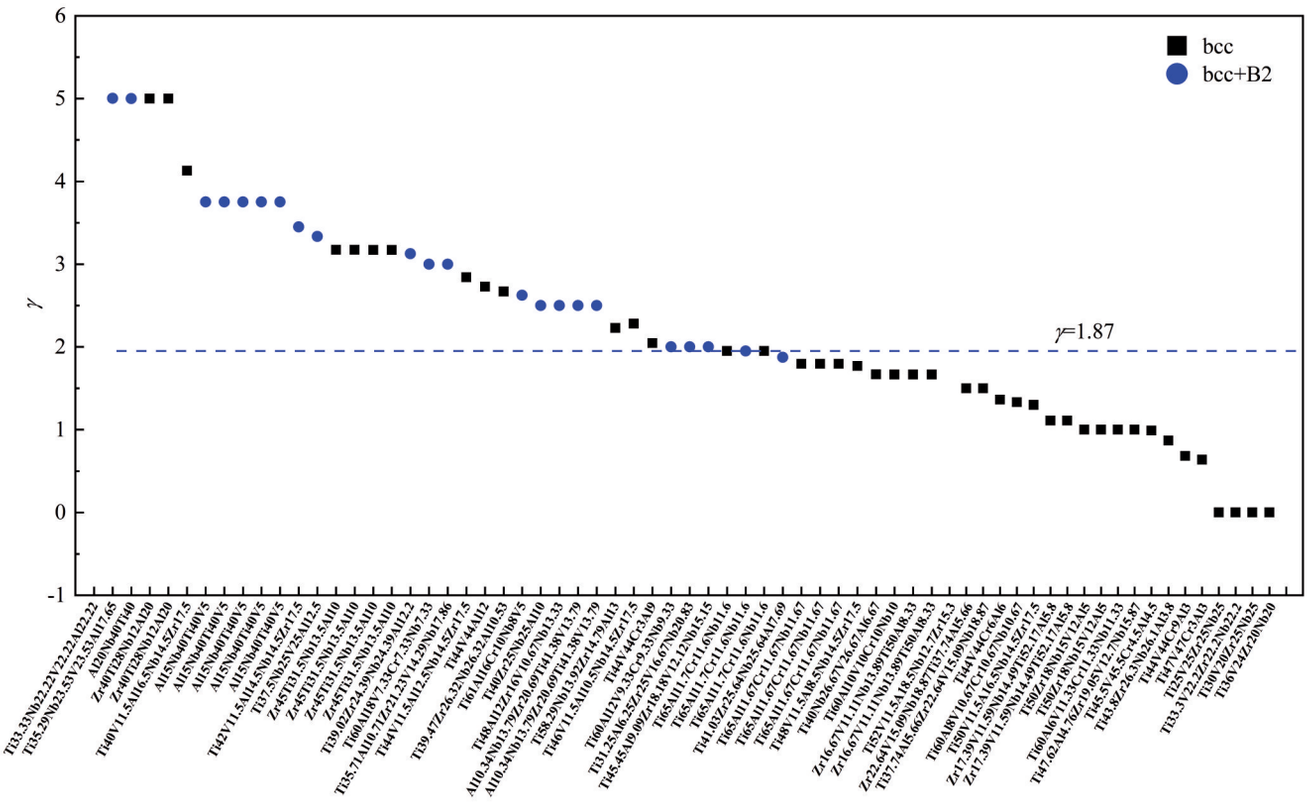

Fig.6 Phase constitution of LWHEAs exhibiting tensile ductility

parameters with mechanical properties of LWHEAs was discussed. Fig. 7 illustrates the relationships between ΔH_{mix} and VEC value in LWHEAs. Interestingly, alloys with tensile ductility can be effectively screened out from these alloy systems without tensile ductility. As shown in Fig. 7, alloys lacking tensile ductility occupy a broader parameter space. It can be known from the statistics that the alloys satisfying the conditions $\Delta H_{mix} \leqslant -6.566$ kJ/mol, VEC≤4.375, and $\Delta H_{mix} > (\Delta H_{mix}+129.5)/\text{VEC}=26.93$ exhibit a high probability of tensile ductility. This criterion, particularly for the alloys containing B2 phase, represents a key requirement for achieving ductility in LWHEAs.

Fig.7 also shows an important indication that both ΔH_{mix} and VEC play important roles in the mechanical properties of LWHEAs. The effect of negative mixing enthalpy on the

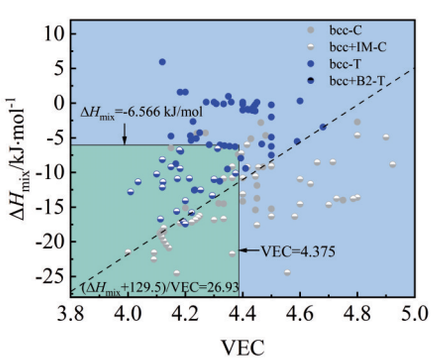

Fig.7 ΔH_{mix} vs. VEC results of LWHEAs with tensile or compressive ductility

mechanical properties of materials is fundamentally governed by its thermodynamic driving force for microstructural evolution, functioning as a classic "double-edged sword". A strongly negative mixing enthalpy promotes chemical ordering or phase separation, thereby facilitating the formation of secondary phases, such as intermetallic compounds (e. g., B2 and Laves phases) or nanoscale precipitates. These hard phases markedly enhance the strength and hardness of the alloy through mechanisms, including order strengthening, precipitation strengthening, and grain-refinement strengthening. Consequently, the controlled introduction of such energetically favorable interactions has become a critical strategy in the design of ultrahigh-strength alloys. For example, in bcc-structured high-entropy alloys, incorporating element pairs with strongly negative mixing enthalpy (Al-Ni or Al-Ti) is often indispensable for achieving yield strengths in the gigapascal range.

However, this strengthening effect is often accompanied by a deterioration in plasticity and toughness. The secondary phases driven by strongly negative mixing enthalpy—particularly continuous intergranular networks or coarse precipitates—are inherently brittle, and they provide favorable sites for crack initiation and propagation. Consequently, materials exhibit pronounced brittleness under tension or impact loading. Thus, a major challenge in contemporary alloy design is to harness the strengthening benefits of negative mixing enthalpy while mitigating its embrittlement tendency. This requires synergistic strategies involving compositional design (e. g., entropy modulation to suppress excessive ordering) and processing control[7] (e.g., refinement,

dispersion, or morphological regulation of precipitates) to achieve a desirable balance between strength and ductility.

Recent studies further demonstrate that increasingly negative mixing enthalpy promotes chemical heterogeneity in solid solutions, including short-range order and local chemical fluctuations[38–39], which can provide promising pathways for enhancing LWHEA's ductility. Elements with negative mixing enthalpy relative to others enhance atomic affinity, thereby favoring chemical segregation or ordering[40–41]. An et al[42] reported that these chemically heterogeneous interfaces not only strengthen the materials but also activate intragranular dislocations and promote their interactions, markedly improving the strain-hardening capacity of LWHEAs.

Meanwhile, VEC serves as a core electronic structure parameter that fundamentally influences material properties by regulating the phase stability and interelectronic interactions in alloys. Its primary role is to determine the crystal structure of the matrix phase[32]: a high VEC (typically VEC≥ 8.0) usually corresponds to stable fcc structure, whose plastic deformation is dominated by dislocation slip, generally endowing the material with excellent ductility and toughness; whereas a low VEC (typically VEC≤ 6.8) is related to bcc structure, which offers high deformation resistance and thus provides exceptional strength and hardness, though often at the expense of restricted ductility. Therefore, VEC acts as a key "electronic building block" for designing alloys with a fundamental performance orientation, whether ductility-dominated or strength-dominated.

Moreover, a clear and crucial inverse correlation exists between VEC and stacking-fault energy (SFE), based on the influence of electronic structure on the stability of atomic stacking at fault planes: a decrease in VEC directly leads to a reduction in SFE. Although deformation in bcc alloys does not directly depend on SFE, precisely tailoring VEC into a lower range (as indicated in Fig. 7, VEC<4.375) facilitates the dissociation of dislocations into extended dislocations, thereby improving the slip resistance. At the same time, a low SFE strongly promotes the activation of transformation-induced plasticity[47], which offers a potential pathway for improving the inferior room-temperature ductility of bcc-structured high-entropy alloys through electronic-structure engineering.

For example, in $(FeCoNi)_3V$ intermetallic alloys with long-range ordered structures, specific sequences of stacked close-packed ordered layers are observed[24]. The stacking behavior can be systematically tuned by adjusting the VEC value. With the decrease in VEC value, achieved by partially substituting Co and Ni with Fe, the long-range-ordered structure evolves from a purely hexagonal phase to an $L1_2$-type cubic ordered structure, passing through intermediate mixed states of hexagonal and cubic layers. Since the hexagonal phase is prone to brittle fracture and the cubic ordered structure is ductile, tailoring VEC value offers an effective approach to optimizing the mechanical properties of long-range-ordered alloys.

For bcc-structured LWHEAs, the intrinsic ductility of perfect crystals plays a pivotal role in determining the mechanical behavior. From the stress perspective, dislocation nucleation requires the local shear stress on a slip plane to approach the ideal shear strength[43], whereas crack initiation occurs when the local tensile stress normal to a cleavage plane exceeds the ideal tensile strength. Notably, even under loading perpendicular to the cleavage plane, certain crystal structures may reach the ideal shear strength along other crystallographic directions firstly, leading to the shear-dominated failure[44]. In such a shear-instability case, dislocation nucleation precedes crack formation, thereby impairing inherent ductility to the material. In bcc metals, the <111> orientation is generally the weakest direction under tensile loading[45]. Group V transition metals, such as V and Nb, undergo shear instability before reaching the ideal tensile strength, leading to the breakdown of tetragonal symmetry and impairing intrinsic ductility. By contrast, Group VI elements, such as Mo and W, experience shear instability only after surpassing the ideal tensile strength, thereby exhibiting intrinsic brittleness[46]. First-principles studies have further revealed that alloying Mo and W to reduce VEC value lowers the Fermi level and promotes partial occupation of degenerate electronic bands. This effect advances the critical strain for shear instability, enabling a brittle-to-ductile transition and thus conferring inherent ductility[47].

The parameter γ can effectively distinguish the ordered B2 phase from random bcc solid solutions. To explore the possible correlations between the parameter γ and mechanical properties, the relationships of specific strength and fracture strain with parameter γ of different LWHEAs are shown in Fig.8. It is obvious that the parameter γ alone is not sufficient to distinguish the tensile or compressive ductility of materials. Previous investigations on the Ti-Al-Nb-V-Zr alloy system

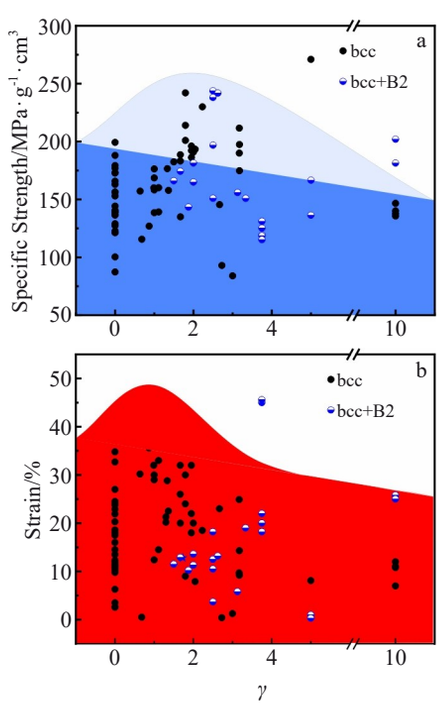

Fig.8 Relationships of specific strength-γ (a) and fracture strain-γ (b) of different LWHEAs

have revealed that the precipitates are primarily intermetallic compounds, which generally improve both room-temperature and high-temperature properties, such as strength and hardness. For example, Wang et al[48] demonstrated that increasing the γ value in the $Ti_{1.6}ZrNbAl_x$ alloy system not only reduced the alloy density but also promoted the formation of coherent nano-sized B2 precipitates. This microstructural refinement substantially improved both yield strength and specific yield strength. Nevertheless, as shown in Fig.8, the strengthening effect of the B2 phase is not limitless: the specific strength peaks at approximately γ =2. Further increase in γ yields no significant improvement in mechanical performance. As the γ value increases, the tensile plasticity of most LWHEAs, except for a certain equiatomic composition, also declines markedly. Representative cases include $Ti_{44}V_{44}Al_{12}$ and $Al_{20}Nb_{40}Ti_{40}$ alloys, which exhibit tensile plastic strains of only 0.4% and 0.3%, respectively[11,49]. The bcc+B2 alloys generally display lower ductility, compared with their single-phase bcc counterparts. For instance, Zhu et al[50] demonstrated that increasing the Al content induces a transition from a disordered bcc to an ordered B2 phase. Although this SRO effect contributes to substantial strengthening and a pronounced increase in yield strength, it simultaneously reduces tensile plasticity from 20% to 1%. Notably, the $Ti_{1.5}NbVAl$ alloy even lost its tensile ductility entirely.

Although an increased γ value generally promotes the formation of secondary phases that severely degrade ductility, careful regulation of γ in combination with optimized thermal treatments can still yield an excellent strength-ductility balance. For instance, Wang et al[18] demonstrated that aging the $Ti_{50}Zr_{18}Nb_{15}V_{12}Al_5$ alloy at 300 °C for 7 d significantly enhanced the degree of B2-like local chemical ordering within the matrix. These ordered regions served as barriers and dispersion sites for slip bands, effectively promoting their multiplication and interaction. As a result, the alloy exhibited a high work-hardening capacity, achieving ultrahigh strength with uniform tensile plasticity. Similarly, Lv et al[19] reported that rapid solidification of an LWHEA led to a fine-grained microstructure containing secondary phase particles uniformly distributed in the matrix, resulting in concurrent improvements in both strength and ductility.

Thus, the ΔH_{mix} and VEC play pivotal roles in dictating the mechanical response of LWHEAs and establish clear design criteria for achieving tensile ductility. These findings not only deepen the understanding of ductility mechanisms in multi-principal element alloys but also provide practical guidance for tailoring alloy composition to meet the requirements of advanced lightweight structural materials. Although γ cannot distinguish whether a material has tensile plasticity or not, it does have a certain influence on the strength and ductility of the material. The strengthening effect introduced by γ-controlled secondary phases is inherently constrained: excessive γ promotes brittle intermetallic precipitation, usually leading to premature loss of ductility. Moreover, the complex interplay among γ, thermodynamic parameters, and processing conditions remains obscure, restricting the predictive accuracy of current design strategies. Future research should therefore aim to refine γ -based criteria by integrating them with advanced thermodynamic modeling and microstructural simulations, as well as investigating the volume fraction, morphology, and spatial distribution of γ -induced second phases. Such efforts are essential to establish a more robust framework for designing LWHEAs with simultaneously high strength, ductility, and thermal stability.

3 Design of LWHEAs with Enhanced Mechanical Properties

This study aims to develop an LWHEA system that exhibits excellent tensile ductility at room temperature along with superior strength. In Ref. [18], it reported that by regulating the B2-like ordered phase, coordination of high plasticity can be effectively achieved. On this basis, the $Ti_{50}Al_{6.5}V_{11.5}Nb_{14.5}Zr_{17.5}$ alloy was selected as the baseline composition and prepared using a magnetically levitated vacuum melting furnace. Guided by the observed correlation between alloy composition and tensile properties in LWHEAs, alloy systems with intentionally reduced γ values were designed to facilitate subsequent control over B2 phase precipitation.

The regulation of B2 precipitation was achieved by varying the γ value within the $Ti_{(50-x)}Al_{(6.5+x)}V_{11.5}Nb_{14.5}Zr_{17.5}$ (x=0, 2, 4, 6, 8, 10) series alloys, which are labeled as $Ti_{(50-x)}Al_{(6.5+x)}$ alloys. The resulting alloys were thoroughly characterized to investigate the influence of composition regulation of B2 phase on microstructural evolution and mechanical behavior.

As shown in Fig. 9a, XRD patterns of the as-cast alloys reveal that all major diffraction peaks correspond to a bcc structure. This structural characteristic remains stable with the

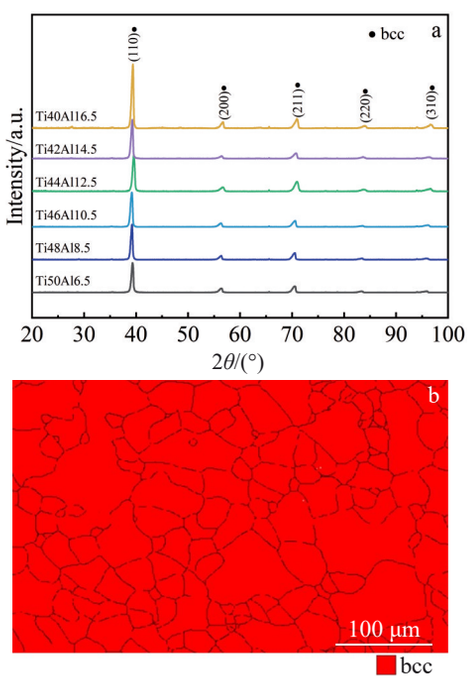

Fig.9 XRD patterns of $Ti_{(50-x)}Al_{(6.5+x)}V_{11.5}Nb_{14.5}Zr_{17.5}$ alloys (a); EBSD phase map of $Ti_{40}Al_{16.5}$ alloy (b)

increase in γ value. A weak diffraction signal observed at the (100) crystal plane suggests the presence of a B2 ordered phase. This finding is corroborated by phase mapping result observed by electron backscattered diffractometer (EBSD), as shown in Fig.9b, which confirms that the alloy series consists predominantly of the single bcc phase. The average diameter (grain size) in the $Ti_{(50-x)}Al_{(6.5+x)}$ alloys is decreased significantly with the increase in γ value, as shown in Fig. 10. This refinement is driven by the elevated Al content, which enhances the formation of the B2 phase and secondary intermetallic compounds. Grain refinement is attributed to the combined mechanisms of heterogeneous nucleation at these precipitates and the Zener pinning effect that suppresses grain boundary migration.

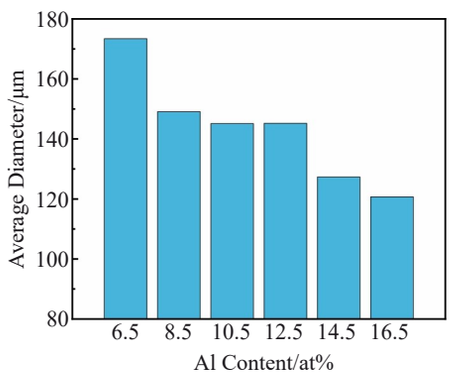

Fig.10 Statistical distribution of average diameter (grain size) of $Ti_{(50-x)}Al_{(6.5+x)}$ alloys

To further elucidate the microstructural evolution, detailed transmission electron microscopy (TEM) analyses, namely high angle angular dark field-scanning transmission electron microscopy (HADDF-STEM) analyses, were performed, as shown in Fig. 11. The corresponding selected-area electron diffraction (SAED) patterns confirm the existence of bcc matrix in all alloys (Fig. 11), consistent with XRD and EBSD findings. In addition to the fundamental bcc reflections, distinct superlattice spots can be observed, and their intensity is increased progressively with the increase in γ value (Fig. 11). Inverse fast Fourier transform (IFFT) images reconstructed from these superlattice reflections (highlighted by yellow circles) reveal diffuse SRO domains in all alloys. Quantitative analysis of SRO area fractions (Fig. 12) shows a clear trend: as γ increases, the SRO domains not only expand in fraction but also interconnect to form larger clusters. These results provide direct evidence that the γ value plays a decisive role in controlling the extent of local chemical ordering, along with its volume fraction and spatial distribution.

The room-temperature tensile properties of different alloys were evaluated. As shown in Fig. 13a, the γ value exerts a pronounced influence on the mechanical behavior. The tensile strength is generally increased with γ, reaching a peak yield strength of 1132 MPa at γ =2.84 ($Ti_{44}Al_{12.5}$), although the ductility is only 1.77%. These alloys achieve a superior strength-ductility balance. Particularly, $Ti_{48}Al_{8.5}$ alloy exhibits a yield strength approaching 1 GPa, while the strength of

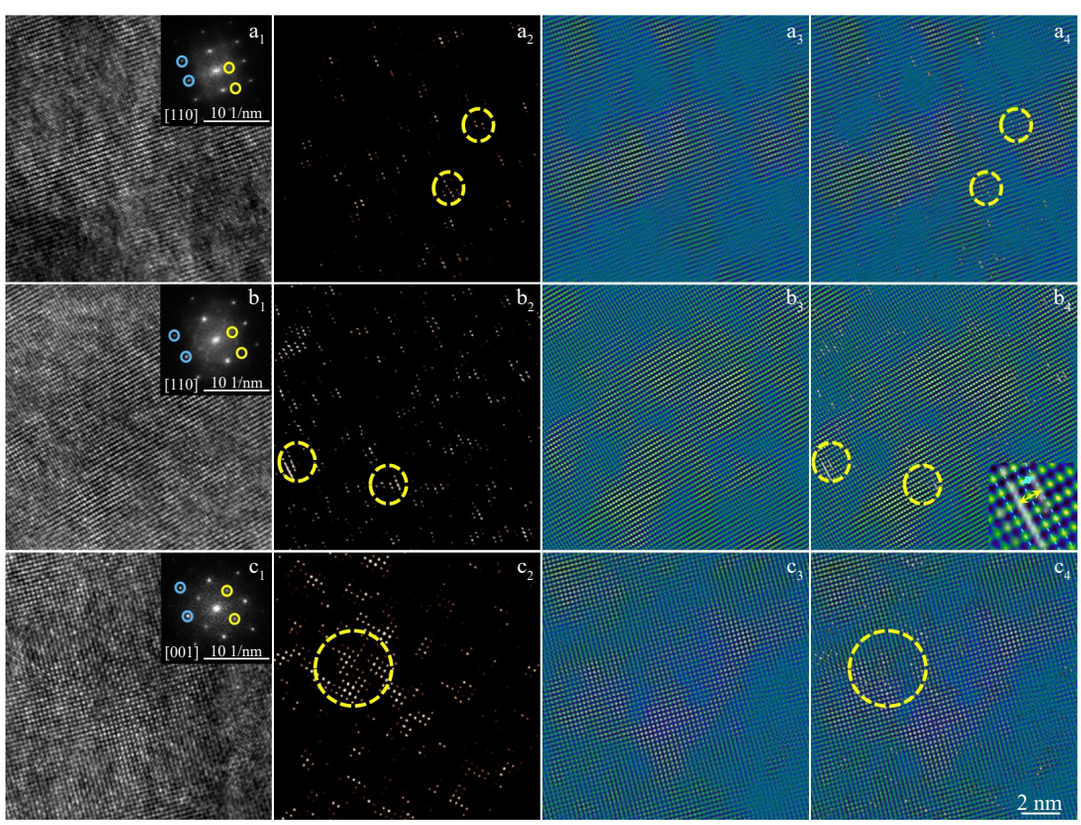

Fig.11 HADDF-STEM analyses of $Ti_{50}Al_{6.5}$ (a_1–a_4), $Ti_{48}Al_{8.5}$ (b_1–b_4), and $Ti_{46}Al_{10.5}$ (c_1–c_4) alloys: (a_1, b_1, c_1) HADDF images with insets of inverse Fourier transform patterns; (a_2, b_2, c_2) IFFT images obtained from superlattice reflections in Fig. 11a_1, 11b_1, and 11c_1; (a_3, b_3, c_3) IFFT images obtained from bcc matrix reflections; (a_4, b_4, c_4) superimposed IFFT images combining the ordered-domain and matrix reflections

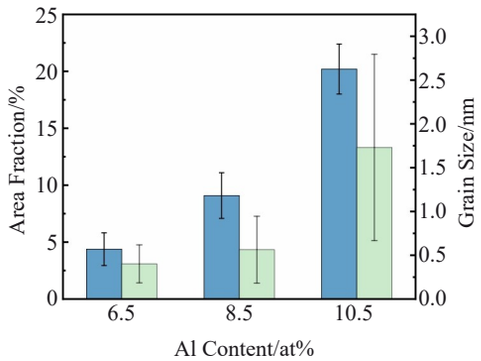

Fig.12 Statistical analysis of SRO area fraction and grain size of different alloy systems

$Ti_{46}Al_{10.5}$ alloy surpasses this threshold with a tensile ductility exceeding 20% (Fig. 13b). It should be noted that the $Ti_{42}Al_{14.5}$ and $Ti_{40}Al_{16.5}$ alloys exhibit negligible plasticity and are therefore omitted from Fig. 13. As illustrated in Fig. 13c, all alloys display a relatively low work-hardening capacity, which remains largely insensitive to the γ value. This behavior can be attributed to the heterogeneous grain structure observed in the $Ti_{50}Al_{6.5}$ and $Ti_{44}Al_{12.5}$ alloys. In such microstructures, fine grains contribute to strain accommodation, whereas coarse grains readily act as stress concentration sites, facilitating crack initiation[51–52]. Consequently, subsequent thermomechanical processing, such as compositional homogenization heat treatments or cold rolling followed by recrystallization annealing, is necessary

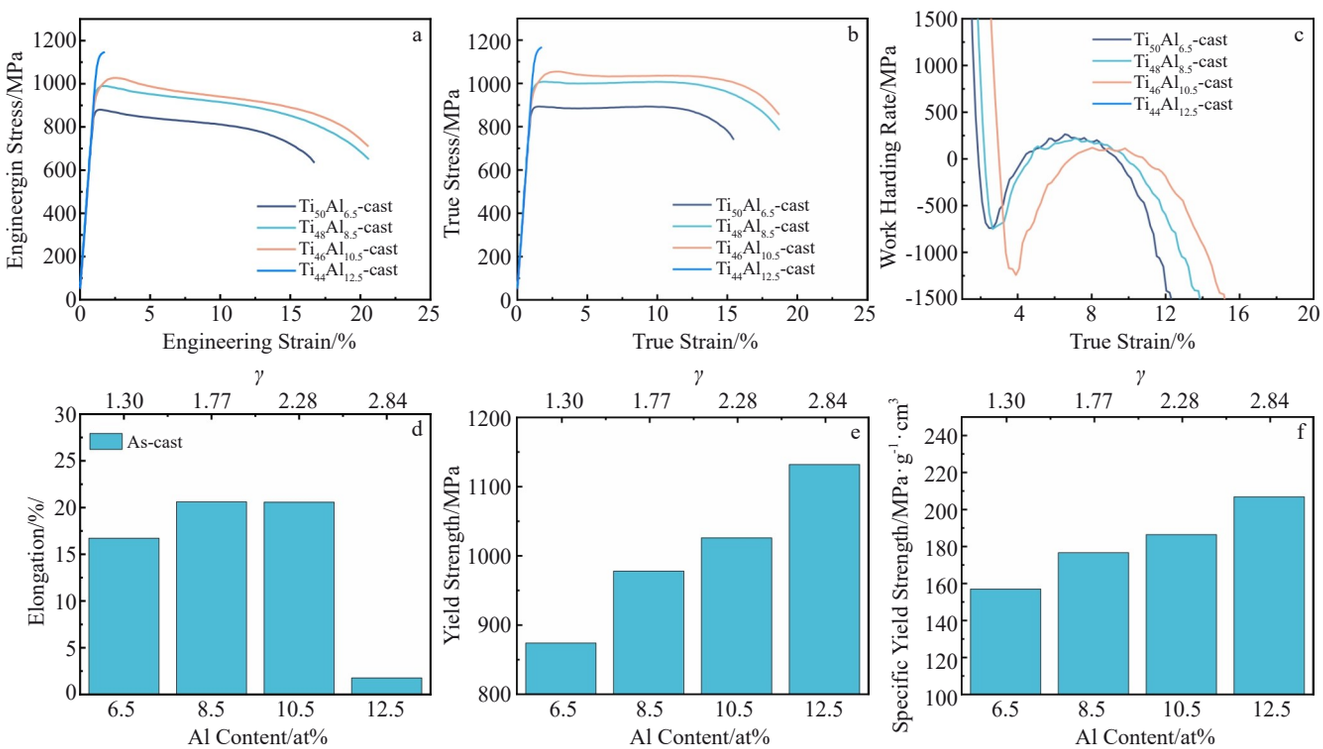

Fig.13 Room-temperature tensile mechanical properties of different alloys: (a) engineering stress-engineering strain curves; (b) true stress-true strain curves; (c) work-hardening rate curves; (d) elongation at break; (e) yield strength; (f) specific yield strength

to achieve an optimized strength-ductility synergy.

Systematic investigation of the Ti-Al-Nb-V-Zr alloy series confirmed the pivotal role of the parameter γ in governing the microstructural evolution and mechanical properties. XRD and EBSD analyses indicate that the as-cast alloys maintain a dominant bcc structure, while TEM characterization reveals the presence of nanoscale B2-like ordered domains, the fraction of which increases progressively with γ. Grain size measurements further demonstrate that elevated γ values promote the precipitation of intermetallic compounds, which refine the microstructure by acting as heterogeneous nucleation sites and grain-boundary pinning agents. Mechanically, although the yield strength is generally increased with the increase in γ, excessive values (>2.0) lead to a severe loss of tensile ductility. The most promising strength-ductility synergy is achieved at a moderate γ value of approximately 2.0 ($Ti_{46}Al_{10.5}$ alloy), whereas the composition with a higher γ results in brittle fracture. These findings collectively demonstrate that γ serves as a decisive compositional parameter for controlling B2 phase formation, microstructural refinement, and the mechanical performance of LWHEAs.

4 Conclusions

1) Although conventional empirical parameters (ΔH_{mix}, VEC, δ, and Φ) offer general guidance for phase stability in LWHEAs, the Al/Ti ratio (γ) emerges as a more decisive and precise criterion for microstructural control. Systematic experiments on Ti-Al-Nb-V-Zr alloy series confirm that γ directly governs B2 phase precipitation, chemical SRO,

and grain refinement. A critical threshold of $\gamma \approx 1.87$ delineates the transition from single-phase bcc to bcc+B2 microstructures. With the increase in γ value, the nanoscale ordering and grain refinement are promoted, yet simultaneously impairing tensile ductility under excessive γ value. The $Ti_{46}Al_{10.5}$ alloy ($\gamma \approx 2.0$) achieves an optimal strength-ductility synergy, demonstrating that integrating γ -specific compositional design with established thermodynamic descriptors provides a practical and effective strategy for developing LWHEAs with tailored microstructures and enhanced mechanical performance.

2) Nevertheless, the γ criterion is not universally applicable without consideration of alloy chemistry. Its predictive capability may be influenced by the presence of strong B2-forming or Laves-forming elements (Nb, Zr, and V), as well as potential synergistic or antagonistic interactions among minor solute additions. Furthermore, γ primarily captures the compositional balance between Al and Ti, while kinetic factors, such as processing history, and local chemical fluctuations also play critical roles in determining the ordering behavior and phase stability. Future studies should therefore focus on quantifying these effects and establishing the γ-based design framework for other LWHEA families beyond the Ti-Al-Nb-V-Zr system. Combining γ with high-throughput thermodynamic calculations, machine-learning-assisted screening, and microstructure-enabled property models is expected to yield a more comprehensive and transferable alloy-design methodology.

Supplement

Table S1 Composition, γ, δ, ΔH_{mix}, VEC, Φ, compressive mechanical properties, and phase composition of LWHEAs

Alloy	γ	δ/%	ΔH_{mix}/kJ·mol^{-1}	VEC	Φ	Stress, σ/MPa	Strain, ε/%	Phase	Ref.
AlMo0.5NbTa0.5TiZr	10	5.04	–16.84	4.3	8.94	2197	4.1	bcc+B2	[53]
AlMo0.5NbTa0.5TiZr0.5	10	4.19	–16.69	4.33	12.77	1320	1	bcc	[53]
AlNbTa0.5TiZr0.5	10	3.82	–18.56	4.13	9.14	1352	1.3	bcc	[53]
Al0.5Mo0.5NbTa0.5TiZr	5	5.24	–10.52	4.44	12.11	2350	3.2	bcc	[53]
Al0.25NbTaTiZr	2.5	4.77	–3.93	4.41	16.35	1745	3.8	bcc	[53]
Al0.5NbTi3V0.5Zr2	1.6	5.70	7.68	4.14	6.88	790	>50	bcc	[54]
Ti40Nb30Hf15Al15	3.75	3.39	–12.27	4.25	14.43	1250	16	bcc+intermetallic compound	[55]
W10Mo27Cr21Ti22Al20	9.09	6.1	–14.66	4.7	5.29	1245	7.7	bcc+intermetallic compound	[56]
Ti2Al0.5VNbMo0.5	2.5	3.99	–9	4.5	17.76	900	50	bcc	[57]
Ti7Al3V4Nb4Mo2	4.29	3.93	–11.88	4.45	15.99	971	50	bcc	[57]
Ti3Al2V2Nb2Mo	6.67	3.86	–14.16	4.4	14.17	1187	10	bcc	[57]
Nb25Mo25Ta25W25	0	2.31	–6.5	5.5	60.98	1058	2.6	bcc	[58]
V20Nb20Mo20Ta20W20	0	3.15	–4.64	5.4	41.17	1246	1.7	bcc	[58]
AlMo0.5NbTa0.5TiZr	10	5.04	–16.84	4.3	8.94	2000	10	bcc1+bcc2	[59]
AlNb1.5Ta0.5Ti1.5Zr0.5	6.67	3.48	–15.12	4.2	14.71	1280	3.5	bcc	[59]
Al0.4Hf0.6NbTaTiZr	4	4.92	–6.33	4.32	16.59	1841	10	bcc	[59]
Al0.3NbTaTi1.4Zr1.3	2.14	4.84	–4.41	4.34	15.44	1965	5	bcc1+bcc2	[59]
Al0.3NbTa0.8Ti1.4V0.2Zr1.3	2.14	5.3	–4.86	4.34	13.76	1965	5	bcc	[59]
Al0.5NbTa0.8Ti1.5V0.2Zr	3.33	4.93	–8.62	4.3	13.9	2035	4.5	bcc1+bcc2	[59]
TaNbHfZrTi	0	4.99	2.72	4.4	16.9	929	38	bcc	[60]
HfMoTaZrTi	0	6.09	–1.92	4.6	11.84	1600	4	bcc	[61]
HfMoNbTaZrTi	0	5.78	–0.89	4.67	14.95	1512	12	bcc	[61]
TiNbMoTaW	0	2.75	–5.28	5.2	52.72	1343	14.1	bcc	[62]
TiVNbMoTaW	0	3.58	–4.22	5.17	36.25	1515	10.6	bcc	[62]
CrMoNbV	0	4.91	–4	5.5	14.25	1501	6	bcc	[63]
HfMo0.5NbTiV0.5	0	5.94	–0.88	4.63	12.38	1260	35	bcc	[64]
HfMo0.5NbTiV0.5Si0.3	0	7.88	–16.37	4.58	4.25	1617	18.5	bcc+intermetallic compound	[64]
HfMo0.5NbTiV0.5Si0.5	0	8.76	–24.44	4.56	1.91	1787	11.9	bcc+intermetallic compound	[64]
HfMo0.5NbTiV0.5Si0.7	0	9.44	–31.12	4.53	0.46	2134	9.2	bcc+intermetallic compound	[64]
Al0.1CrNbVMo	0	4.96	–4.97	5.44	14.35	2863	8.6	bcc	[65]
AlNbTiV	10	3.95	–16.25	4.25	7.22	1000	5.2	bcc	[66]
AlCr0.5NbTiV	10	5.23	–15.41	4.44	6.94	1300	0.8	bcc	[66]
AlCrNbTiV	10	5.9	–14.56	4.6	6.18	1550	0.4	bcc+Laves	[66]

Continued table

Alloy	γ	δ/%	ΔH_{mix}/kJ·mol^{-1}	VEC	Φ	Stress, σ/MPa	Strain, ε/%	Phase	Ref.
AlCr1.5NbTiV	10	6.29	–13.75	4.73	6.29	1700	0	bcc+Laves	[66]
AlNbTiVZr0.1	10	4.42	–16.51	4.24	6.65	1290	-	B2+hcp-Al_3Zr_5	[9]
AlNbTiVZr0.25	10	4.97	–16.83	4.24	5.73	1360	-	B2+hcp-Al_3Zr_5	[9]
AlNbTiVZr	10	6.35	–17.44	4.2	3.91	1500	-	bcc+intermetallic compound	[9]
AlNbTiVZr1.5	10	6.72	–17.32	4.18	3.51	1535	-	bcc+intermetallic compound	[9]
Al0.5CrNbTi2V0.5	2.5	6.02	–10.96	4.6	6.88	1340	18.5	bcc+intermetallic compound	[67]
CrMo0.5NbTa0.5TiZr	0	8.04	–4.92	4.9	6.81	1595	-	bcc+Laves	[68]
HfMoNbTiZr	0	6.1	–1.6	4.6	11.89	1719	-	bcc	[69]
HfNbSi0.5TiVZr	0	9.42	–21.75	4.36	2.07	1540	-	bcc+Laves+M_5Si_3	[70]
Al2NbTi1.0V2Zr	19.99	6.32	–20.9	4.14	1.42	2134	16.4	bcc+Zr_3Al	[71]
Al2NbTi1.5V2Zr	13.34	6.12	–20.41	4.13	1.89	2109	17.5	bcc+Zr_3Al	[71]
Al2NbTi2.0V2Zr	10	5.95	–19.88	4.13	2.27	2068	21.5	bcc+Zr_3Al+Ti_2ZrAl	[71]
Al2NbTi2.5V2Zr	8	5.78	–19.32	4.12	2.6	2082	21.9	bcc+Zr_3Al+Ti_2ZrAl	[71]
Al2NbTi3.0V2Zr	6.67	5.63	–18.77	4.11	2.89	2153	19.8	bcc+Zr_3Al+Ti_2ZrAl	[71]
Al0.5CrNbTi2V0.5	2.5	6.02	–10.96	4.6	6.88	1240	>50	bcc	[47]
AlNbTiV	10	3.95	–16.25	4.25	7.22	1020	5	bcc	[12]
Al0NbTiVZr	0	7.05	–0.25	4.5	7.97	1320	4.2	bcc+Laves	[8]
Al0.5NbTiVZr	5	6.67	–10.86	4.33	6.18	960	4	bcc+Laves+Zr_2Al	[8]
AlNbTiVZr	10	6.35	–17.44	4.2	3.91	1080	2.3	bcc+Laves+Zr_2Al	[8]
Al1.5NbTiVZr	15	6.07	–21.55	4.09	1.71	1310	0	bcc+Laves+Zr_2Al	[8]
Al24Cr11Nb11Ti37Zr17	6.49	6.39	–22.54	4.09	0.18	1570	0	bcc+Laves+B2	[72]
Al20Cr20Nb25Ti25Zr10	8	6.93	–17.58	4.45	3.14	1830	0.7	bcc+Laves+B2	[72]
Al28Cr15Nb15Ti20Zr22	14	7.37	–24.55	4.17	–0.07	795	0	bcc+Laves+B2	[72]
Al0CrNbTiVZr	0	8.68	–4.64	4.8	5.24	1260	0.2	bcc+Laves	[10]
Al0.25CrNbTiVZr	2.5	8.47	–8.49	4.71	5.07	1095	0	bcc+Laves	[10]
Al0.5CrNbTiVZr	5	8.27	–11.64	4.64	4.69	1630	0	bcc+Laves	[10]
AlCrNbTiVZr	10	7.92	–16.33	4.5	3.78	850	0	bcc+Laves	[10]
Al0.4NbTiV	10	4.23	–9.2	4.47	13.26	928	>30	bcc	[73]
Al0.8NbTiV	8	4.04	–14.46	4.32	9.24	1133	>30	bcc	[73]
AlNbTiV	10	3.95	–16.25	4.25	7.22	1379	20.9	bcc	[73]
AlNb2TiV	10	3.56	–13.12	4.4	13.54	1043	>33	bcc+B2	[74]
Ti3V2NbAl0.5	1.67	4.52	–7.38	4.38	11.1	760	>50	bcc	[75]
Ti3V2NbNi0.5	1.67	5.49	–8.85	4.92	6.85	1130	20	bcc+Laves (C15)	[75]
Ti3V2NbAl0.5Ni0.5	1.67	5.33	–13.8	4.79	5.82	1250	40	bcc+intermetallic compound	[75]
AlNbTiZr	10	4.81	–21.5	4	0.59	1250	8.6	bcc+B2	[76]
AlNbTiZr	10	4.81	–21.5	4	0.59	1509	17.8	bcc+B2+Laves	[76]
Al0.1NbTiVZr	1	6.97	–2.81	4.46	7.8	1177	19.4	bcc	[77]
Al0.2NbTiVZr	2	6.89	–5.12	4.43	7.45	1242	11.94	bcc	[77]
Al0.3NbTiVZr	3	6.81	–7.23	4.4	7.05	1367	10.14	bcc+Laves	[77]
Al0.4NbTiVZr	4	6.74	–9.13	4.36	6.62	1298	9.29	bcc+Laves	[77]
Al0.5NbTiVZr	5	6.67	–10.86	4.33	6.18	1264	6.15	bcc+Laves	[77]
Al0.5NbTiV2Zr0.5	5	6.32	–9.12	4.5	6.74	1390	16.9	bcc+Laves	[78]
Al0.5NbTiV2Zr	5	7.13	–9.26	4.45	5.54	1028	9.3	bcc+Laves	[78]
Al0.5NbTiV2Zr1.5	5.19	7.56	–9.22	4.42	4.98	641	5.5	bcc+Laves	[78]
Al0.5Nb0.5TiV2Zr0.5	5	6.65	–10.57	4.44	5.14	1480	14.1	bcc+Laves	[78]
Al0.5Nb0.5TiV2Zr	5	7.48	–10.8	4.4	4.27	1251	7.3	bcc+Laves	[78]
Al0.5Nb0.5TiV2Zr1.5	5	7.89	–10.78	4.36	3.88	797	5.1	bcc+ Laves	[78]
NbTiVZr	0	7.05	–0.25	4.5	7.97	1110	>50	bcc	[79]

Continued table

Alloy	γ	δ/%	ΔH_{mix}/kJ·mol^{-1}	VEC	Φ	Stress, σ/MPa	Strain, ε/%	Phase	Ref.
NbTiVZrMo	0	6.85	–2.72	4.8	8.89	1510	9.3	bcc+Laves	[79]
NbTiVZrTa	0	6.35	0.32	4.6	11.28	1395	19.1	bcc	[79]
NbTiVZrCr	0	8.68	–4.64	4.8	5.24	1295	2.8	bcc+Laves	[79]
NbTiVZrAl0.24	2.4	6.86	–5.99	4.42	7.3	1240	5.4	bcc+Laves	[79]
Ti1.5ZrVNb	0	6.64	–0.2	4.44	8.86	1119	50	bcc	[80]
Ti2ZrVNb	0	6.3	–0.16	4.4	9.59	1086	50	bcc	[80]
Ti20(AlCrVNb)80	10	5.9	–14.56	4.6	6.18	-	-	bcc	[81]
Ti40(AlCrVNb)60	3.75	5.67	–13.74	4.45	6.21	1122	27	bcc	[81]
Ti60(AlCrVNb)40	2.5	5.02	–11.04	4.3	6.61	821	50	bcc	[81]
Ti80(AlCrVNb)20	0.63	3.79	–6.46	4.15	8.06	600	50	bcc	[81]

Table S2 Composition, γ, δ, ΔH_{mix}, VEC, Φ, tensile mechanical properties, and phase composition of LWHEAs

Alloy	γ	δ/%	ΔH_{mix}/kJ·mol^{-1}	VEC	Φ	Stress, σ/MPa	Strain, ε/%	Phase	Ref.
(TiV)88Cr12	0	5.99	–3.45	4.68	6.25	1042	2.6	bcc	[11]
(TiV)88Cr9Al3	0.68	5.8	–5.51	4.59	6.19	600	0.5	bcc	[11]
(TiV)88Cr6Al6	1.36	5.57	–7.50	4.50	5.68	800	22.5	bcc	[11]
(TiV)88Cr3Al9	2.04	5.31	–9.42	4.41	4.79	959	7.9	bcc+B2	[11]
(TiV)88Al12	2.72	5.01	–11.26	4.32	3.14	450	0.4	bcc+B2	[11]
(TiV)91Cr4.5Al4.5	0.98	5.50	–6.24	4.50	5.96	809	32	bcc	[11]
(TiV)94Cr3Al3	0.63	5.42	–4.91	4.50	6.19	800	30.2	bcc	[11]
TiV	0	6.02	–2.00	4.50	5.26	725	17.5	bcc	[11]
Ti65Al11.7Cr11.6Nb11.6	1.8	4.68	–12.56	4.23	3.54	1000	18	bcc	[82]
Ti65Al11.7Cr11.6Nb11.6	1.8	4.68	–12.56	4.23	3.54	980	22	bcc	[82]
Ti60Al6(VCrNb)34	1	4.68	–12.56	4.23	3.54	950	32	bcc+B2	[83]
Ti60Al8(VCrNb)32	1.33	5.28	–7.94	4.39	8.03	895	29	bcc+B2	[83]
Ti60Al10(VCrNb)30	1.66	5.15	–9.52	4.34	7.38	920	28.8	bcc+B2	[83]
Ti60Al12(VCrNb)28	2	5.02	–11.04	4.30	6.61	938	26	bcc+B2	[83]
Zr1.2V0.8NbTi3.6Al0.3	2.5	4.88	–12.54	4.88	5.66	960	20	bcc+B2	[7]
Zr1.2V0.8NbTi3.6Al0.6	5	5.35	–4.69	4.22	10.40	850	33	bcc+B2	[7]
Zr1.2V0.8NbTi2Al0.3	1.5	5.26	–8.75	4.17	8.81	1000	32	bcc+B2	[7]
V0.5Nb0.5ZrTi	0	6.10	–6.00	4.28	8.70	1100	39	bcc	[84]
V0.5Nb0.5ZrTi	0	6.78	–0.11	4.33	8.39	832	18.6	bcc	[84]
Ti43.3V28Zr14Nb14Mo0.7	0	6.78	–0.11	4.33	8.39	787	21.9	bcc	[85]
Ti1.5ZrNbAl0.3	2	6.34	–1.05	4.43	8.90	1045	24.5	bcc	[86]
Ti1.6ZrNbAl0.15	0.93	4.71	–6.95	4.18	11.07	876	23	bcc	[87]
Ti3Zr1.5Nb	0	4.68	–2.65	4.23	13.43	763	35.6	bcc	[88]
Ti3Zr1.5NbV	0	4.52	1.59	4.18	12.43	505.4	16	bcc	[88]
Ti3Zr1.5NbV2	0	6.10	–0.09	4.31	9.82	707.6	9.8	bcc	[88]
TiVZrNb	0	6.76	–1.00	4.40	7.90	974	6.3	bcc	[89]
Ti1.5VZrNb	0	7.05	–0.25	4.50	7.97	900	11	bcc	[89]
(Ti1.5V)2ZrNb	0	6.64	–0.20	4.44	8.86	828	20.3	bcc	[89]
(Ti1.5V)3ZrNb	0	6.68	0.12	4.45	8.86	877	22.9	bcc	[89]
(Ti1.5V)4ZrNb	0	6.60	–0.44	4.44	8.80	782	34.8	bcc	[89]
(Ti1.5V)5ZrNb	0	6.49	–0.76	4.43	8.69	799	27	bcc	[89]
Ti61Al16Cr10Nb8V5	2.62	6.38	–0.98	4.43	8.62	761	24.1	bcc+B2	[90]
(Ti67Nb16Zr17)87Al13	2.23	4.72	–15.63	4.17	2.39	1168	13.2	bcc	[91]
TiZrNbVAl	10	3.75	–12.80	4.01	6.80	1180	18.5	bcc	[16]
(TiZrNbVAl)99.8Y0.2	10	6.35	–17.44	4.20	3.91	808.3	11	bcc	[16]

Continued table

Alloy	γ	δ/%	ΔH_{mix}/kJ·mol^{-1}	VEC	Φ	Stress, σ/MPa	Strain, ε/%	Phase	Ref.
(TiZrNbVAl)99.6Y0.4	10	6.43	–17.32	4.20	3.93	842.8	12	bcc	[16]
(TiZrNbVAl)99.4Y0.6	10	6.51	–17.20	4.20	3.93	790.6	10.8	bcc	[16]
Ti1.5NbVAl0.25	1.66	6.59	–17.07	4.19	3.92	778.3	7	bcc+B2	[50]
Ti1.5NbVAl0.5	3.33	4.23	–5.90	4.47	15.17	800	20	bcc+B2	[50]
Ti1.5NbVAl0.75	5	4.10	–10.13	4.38	12.82	857	19	bcc+B2	[50]
Ti50Zr18Nb15V12Al5	1	3.99	–13.34	4.29	10.27	921	1	bcc+B2	[18]
Ti50Zr18Nb15V12Al5	1	5.44	–5.37	4.22	9.99	870	30	bcc+B2	[18]
Al15Nb40Ti40V5	3.75	5.44	–5.37	4.22	9.99	970	46.7	bcc+B2	[92]
Al15Nb40Ti40V5	3.75	2.21	–10.96	4.30	32.99	785	45	bcc+B2	[92]
Al15Nb40Ti40V5	3.75	2.21	–10.96	4.30	32.99	715	22	bcc+B2	[92]
Al15Nb40Ti40V5	3.75	2.21	–10.96	4.30	32.99	710	20	bcc+B2	[92]
Nb40Ti40V20	0	2.21	–10.96	4.30	32.99	690	18.2	bcc	[49]
Al15Nb40Ti40V5	3.75	3.79	0.32	4.60	21.29	650	32.7	bcc	[49]
Al20Nb40Ti40	5	2.21	–10.96	4.30	32.99	750	45.6	bcc	[49]
(Ti44V28Zr14Nb14)98.5Mo1.5	0	1.09	–14.08	4.20	55.78	795	0.3	bcc+intermetallic compound	[17]
(Ti44V28Zr14Nb14)98.5Mo1.5	0	6.31	–1.14	4.44	9.11	1116	23.8	bcc+intermetallic compound	[17]
Ti44V28Zr14Nb14	0	6.31	–1.14	4.44	9.11	970	14.5	bcc+intermetallic compound	[17]
Ti22Sc22Zr22Nb17V17	0	6.32	–0.96	4.42	8.73	887	18	bcc+fcc+intermetallic compound	[93]
Ti22Sc22Zr22Nb17V17	0	7.77	5.95	4.12	6.17	751	10.22	bcc+fcc+intermetallic compound	[93]
Ti22Sc22Zr22Nb17V17	0	7.77	5.95	4.12	6.17	936	10.71	bcc+fcc+intermetallic compound	[93]
Ti1.6ZrNbAl0.2V0.2	1.25	4.64	–9.20	4.15	9.86	865	12.8	bcc	[94]
Ti1.6ZrNbV0.4	0	5.24	–4.27	4.25	11.59	806	13.2	bcc	[94]
Ti1.6ZrNbAl0.3	1.87	5.76	0.98	4.35	10.69	770	14.8	bcc+B2	[48]
Ti1.6ZrNbAl0.4	2.5	4.66	–6.79	4.18	11.29	843	10.2	bcc+B2	[48]
Ti1.6ZrNbAl0.5	3.12	4.64	–9.20	4.15	9.86	877	10.5	bcc+B2	[48]
(Zr0.5Ti0.35Nb0.15)90Al10	2.22	4.62	–11.37	4.12	8.47	895	5.8	bcc+B2	[95]
(Zr0.5Ti0.35Nb0.15)90Al10	2.22	5.12	–11.36	4.04	6.02	1012	14.3	bcc+B2	[95]
(Zr0.5Ti0.35Nb0.15)80Al20	5	5.12	–11.36	4.04	6.02	1143	9.2	bcc+B2	[95]
(Zr0.5Ti0.35Nb0.15)80Al20	5	5.18	–21.49	3.58	–0.59	-	-	bcc+B2	[95]
(Zr0.5Ti0.35Nb0.15)90Al10	5	5.18	–21.49	3.58	–0.59	1512	8.1	bcc+B2	[95]
(Zr0.5Ti0.35Nb0.15)90Al10	5	5.12	–11.36	4.04	6.02	1225	9.7	bcc+B2	[95]
TiZrAlNbV	10	5.12	–11.36	4.04	6.02	1100	24.9	bcc+B2	[14]
TiZrAlNbV	10	6.35	–17.44	4.20	3.91	943	25.8	bcc+B2	[14]
Ti65(AlCrNb)35	1.79	6.35	–17.44	4.20	3.91	1050.4	25	bcc	[96]
Ti65(AlCrNb)35	1.79	4.68	–12.52	4.23	3.58	1240	25	bcc	[96]
Al10Cr10Ti70V10	1.42	5.09	–12.04	4.20	2.01	877	1.1	bcc	[97]
TiZrVNb	0	7.05	–0.25	4.50	7.97	1116	3.5	bcc	[80]
Ti1.5ZrVNb	0	6.64	–0.20	4.44	8.86	1101	11.2	bcc	[80]
Ti2ZrVNb	0	6.30	–0.16	4.40	9.59	1058	12.3	bcc	[80]

References

1 Cole G, Sherman A. *Materials Characterization*[J], 1995, 35(1): 3

2 Shi Y Z, Yang B, Liaw P K. *Metals*[J], 2017, 7(2): 43

3 Joele M, Matizamhuka W R. *Materials*[J], 2021, 14(19): 5835

4 You X, Song J J, Lin P Y *et al. Tribology Intenational*[J], 2022, 175: 107801

5 Yeh J W, Chen S K, Lin S J *et al. Advanced Engineering Materials*[J], 2004, 6(5): 299

6 Wang X F, He Q F, Wang Y W *et al. cMat*[J], 2025, 2: e70014

7 Wang L, Chen S S, Li B L *et al. Materials Science and Engineering A*[J], 2021, 814: 141234

8 Stepanov N, Yurchenko N Y, Shaysultanov D *et al. Materials Science and Technology*[J], 2015, 31: 1184

9 Yurchenko N Y, Stepanov N, Zherebtsov S *et al. Materials Science and Engineering A*[J], 2017, 704: 82

10 Yurchenko N Y, Stepanov N, Shaysultanov D *et al. Materials Characterization*[J], 2016, 121: 125

11 Li D, Dong Y G, Zhang Z Q *et al. Journal of Alloys and Compounds*[J], 2021, 877: 160199

12 Stepanov N, Shaysultanov D, Salishchev G *et al. Materials Letters*[J], 2015, 142: 153

13 Zherebtsov S, Yurchenko N, Panina E *et al. Intermetallics*[J], 2020, 116: 106652

14 Liu F X, Chen S S, Wang B P *et al. Materials Science and Engineering A*[J], 2022, 861: 144346

15 Klimenko D, Yurchenko N Y, Stepanov N *et al. Materials Today: Proceedings*[J], 2021, 38(4): 1535

16 Cui J X, Yang M, Liu G L *et al. Journal of Alloys and Compounds*[J], 2024, 970: 172734

17 Jia Y F, Ren C, Wu S W *et al. Journal of Materials Science & Technology*[J], 2023, 149: 73

18 Wang L, Ding J, Chen S S *et al. Nature Materials*[J], 2023, 22: 950

19 Lv X, Zhang H, Li Z *et al. Journal of Alloys and Compounds*[J], 2024, 994: 174689

20 Yeh J W, Chen S K, Lin S J *et al. Advanced Engineering Materials*[J], 2004, 6(5): 299

21 Zhang Y, Zhou Y J, Lin J P *et al. Advanced Engineering Materials*[J], 2008, 10(6): 534

22 Feng R, Gao M C, Lee C *et al. Entropy*[J], 2016, 18(9): 333

23 Yang X, Zhang Y. *Materials Chemistry and Physics*[J], 2012, 132(2–3): 233

24 Guo S, Ng C, Lu J *et al. Journal of Applied Physics*[J], 2011, 109(10): 103505

25 Senkov O, Scott J, Senkova S *et al. Journal of Materials Science*[J], 2012, 47: 4062

26 Youssef K M, Zaddach A J, Niu C *et al. Materials Research Letters*[J], 2015, 3(2): 95

27 Ye Y F, Wang Q, Lu J *et al. Materials Today*[J], 2016, 19(6): 349

28 Miracle D B, Senkov O N. *Acta Materialia*[J], 2017, 122: 448

29 Zhang W R, Liaw P K, Zhang Y. *Science China Materials*[J], 2018, 61: 2

30 Sohn S S, Kwiatkowski da Silva A, Ikeda Y *et al. Advanced Materials*[J], 2019, 31: 1807142

31 Chang X, Zeng M, Liu K *et al. Advanced Materials*[J], 2020, 32: 1907226

32 Hsu W L, Tsai C W, Yeh A C *et al. Nature Reviews Chemistry*[J], 2024, 8: 471

33 Smekhova A, Kuzmin A, Siemensmeyer K *et al. Journal of Alloys and Compounds*[J], 2022, 920: 165999

34 Gao M C, Yeh J W, Liaw P K *et al. High-Entropy Alloys: Fundamentals and Applications*[M]. Berlin: Springer, 2016

35 Yin K X, Huang Z W, Wu B L *et al. Acta Materialia*[J], 2024, 263: 119445

36 Zhang Y, Zuo T T, Tang Z *et al. Progress in Materials Science*[J], 2014, 61: 1

37 Dou W, Xu Z J, Hu H Z *et al. International Journal of Impact Engineering*[J], 2021, 155: 103897

38 Ding J, Yu Q, Asta M *et al*. *Proceedings of the National Academy of Sciences*[J], 2018, 115: 8919

39 Bu Y Q, Wu Y, Lei Z F *et al. Materials Today*[J], 2021, 46: 28

40 Ding Q Q, Zhang Y, Chen X *et al. Nature*[J], 2019, 574(7777): 223

41 Chen X F, Wang Q, Cheng Z Y *et al. Nature*[J], 2021, 592(7856): 712

42 An Z B, Li A, Mao S C *et al. Nature*[J], 2024, 625(7996): 697

43 Kelly A, Macmillan N. *Strong Solids*[M]. Oxford: Clarendon Press, 1987

44 Morris J J, Krenn C. *Philosophical Magazine A*[J], 2000, 80(12): 2827

45 Milstein F, Chantasiriwan S. *Physical Review B*[J], 1998, 58(10): 6006

46 Luo W, Roundy D, Cohen M L *et al. Physical Review B*[J], 2002, 66: 094110

47 Qi L, Chrzan D. *Physical Review Letters*[J], 2014, 112: 115503

48 Wang H, Chen W P, Chu C L *et al. Materials Science and Engineering A*[J], 2023, 885: 145661

49 Yurchenko N, Panina E, Tojibaev A *et al. Journal of Alloys and Compounds*[J], 2023, 937: 168465

50 Zhu C, Li X, Zhang Z. *Vacuum*[J], 2024, 221: 112888

51 Kacher J, Eftink B P, Cui B *et al. Current Opinion in Solid State and Materials Science*[J], 2014, 18(4): 227

52 Ondicho I, Alunda B, Park N. *Intermetallics*[J], 2021, 136: 107239

53 Senkov O N, Jensen J K, Pilchak A L *et al. Materials & Design*[J], 2018, 139: 498

54 Wang T T, Jiang W T, Wang X B *et al. Journal of Materials Research and Technology*[J], 2023, 24: 1733

55 Yurchenko N, Panina E, Tikhonovsky M *et al. International Journal of Refractory Metals and Hard Materials*[J], 2020, 92: 105322

56 Naser-Zoshki H, Kiani-Rashid A R, Vahdati-Khaki J. *Vacuum*[J], 2020, 181: 109614

57 Xu Z Q, Ma Z L, Wang M *et al. Materials Science and Engineering A*[J], 2019, 755: 318

58 Senkov O N, Wilks G B, Scott J M *et al. Intermetallics*[J], 2011, 19(5): 698

59 Senkov O N, Woodward C, Miracle D B. *JOM*[J], 2014, 66: 2030

60 Senkov O N, Scott J M, Senkova S V *et al. Journal of Materials Science*[J], 2012, 47(9): 4062

61 Juan C C, Tsai M H, Tsai C W *et al. Intermetallics*[J], 2015, 62: 76

62 Han Z D, Chen N, Zhao S F *et al. Intermetallics*[J], 2017, 84: 153

63 Feng R, Feng B, Gao M C *et al. Advanced Materials*[J], 2021, 33: 2102401

64 Liu Y, Zhang Y, Zhang H *et al. Journal of Alloys and Compounds*[J], 2017, 694: 869

65 Kang B, Lee J, Ryu H J *et al. Journal of Alloys and Compounds*[J], 2018, 767: 1012

66 Stepanov N, Yurchenko N Y, Skibin D *et al. Journal of Alloys and Compounds*[J], 2015, 652: 266

67 Stepanov N, Yurchenko N Y, Panina E *et al. Materials Letters*[J], 2017, 188: 162

68 Senkov O, Woodward C. *Materials Science and Engineering A*[J], 2011, 529: 311

69 Guo N N, Wang L, Luo L S *et al. Materials & Design*[J], 2015, 81: 87

70 Zhang Y, Liu Y, Li Y X *et al. Materials Letters*[J], 2016, 849: 76

71 Zhi Q, Tan X R, Xie J L *et al. Journal of Materials Engineering and Performance*[J], 2022, 31: 4934

72 Yurchenko N, Panina E, Salishchev G *et al. IOP Conference Series: Materials Science and Engineering*[J], 2021, 1014: 012058

73 Lee K, Jung Y, Han J *et al. Materials*[J], 2021, 14(8): 2085

74 Zhu X P, Gao N, Bai Z C *et al. Materials Letters*[J], 2022, 325: 132897

75 Yao H W, Liu Y M, Sun X H *et al. Intermetallics*[J], 2021, 133: 107187

76 Chen W, Tang Q H, Wang H *et al. Materials Science and Technology*[J], 2018, 34(11): 1309

77 Xu J L, Wang T, Lu Y F *et al. Materials Science and Technology*[J], 2020, 36(16): 1762

78 Jiang W T, Wang X H, Kang H J *et al. Journal of Alloys and Compounds*[J], 2022, 925: 166767

79 Senkov O, Rao S, Chaput K *et al. Acta Materialia*[J], 2018, 151: 201

80 Huang T D, Wu S Y, Jiang H *et al. International Journal of Minerals, Metallurgy and Materials*[J], 2020, 27: 1318

81 Zhang X K, Huang J C, Lin P H *et al. Journal of Alloys and Compounds*[J], 2020, 831: 154742

82 Liao Y C, Li T H, Tsai P H *et al. Intermetallics*[J], 2020, 117: 106673

83 Liao Y C, Ye W T, Chen P S *et al. Intermetallics*[J], 2021, 135: 107213

84 Chen Y W, Xu Z Q, Wang M *et al. Materials Science and Engineering A*[J], 2020, 792: 139774

85 Jia Y F, Wu S W, Mu Y K *et al. Advanced Science*[J], 2023, 10(12): 2207535

86 Pang J Y, Zhang H W, Zhang L *et al. Materials Letters*[J], 2021, 290: 129428

87 Wang H, Chen W P, Lu Y M *et al. Materials Science and Engineering A*[J], 2024, 900: 146513

88 Xiao Y K, Peng X H. *Journal of Materials Research and Technology*[J], 2023, 27: 330

89 Jia Y F, Li G C, Ren C *et al. Journal of Materials Science & Technology*[J], 2025, 206: 234

90 He Y Y, Liu Y F, Wang H K *et al. Journal of Alloys and Compounds*[J], 2024, 992: 174522

91 Zhang Y G, Bu Z Q, Yao T T *et al. Journal of Alloys and Compounds*[J], 2023, 936: 168290

92 Yurchenko N, Panina E, Tojibaev A *et al. Materials Science and Engineering A*[J], 2023, 874: 145073

93 Gao Q W, Liu P P, Gong J H *et al. Materials Characterization*[J], 2023, 202: 113025

94 Wang H, Chen W P, Fu Z Q *et al. International Journal of Refractory Metals and Hard Materials*[J], 2023, 116: 106331

95 Yan X H, Liaw P K, Zhang Y. *Journal of Materials Science & Technology*[J], 2022, 110: 109

96 Liao Y C, Chen P S, Tsai P H *et al. Results in Materials*[J], 2022, 16: 100342

97 Huang X J, Miao J S, Luo A A. *Scripta Materialia*[J], 2022, 210: 114462

铝/钛比对钛铝基轻质高熵合金相稳定性和力学性能的影响

罗峰林[1,2]，赫全锋[2]，王旭凤[2]，张　祎[2]，王一伟[2]，况翔益[1,2]，顾剑锋[2]，王　庆[1]

(1. 上海大学 材料研究所，上海 200072)

(2. 上海交通大学 材料科学与工程学院 材料改性与数值模拟研究所，上海 200240)

摘　要：轻质高熵合金是用于先进结构应用的一类极具前景的材料。然而，要精确控制其相形成过程和力学性能仍是一项重大挑战。尽管常规的经验参数（混合焓ΔH_{mix}、价电子浓度、原子尺寸差异δ、电负性差值Φ）为Ti-Al基轻质高熵合金的相稳定性提供了通用指导，但它们的预测准确性是有限的。Al/Ti原子比（γ，即铝/钛比）是精确控制微观结构的关键准则。基于此参数，设计并合成了一系列$Ti_{(50-x)}Al_{(6.5+x)}V_{11.5}Nb_{14.5}Zr_{17.5}$合金。结果表明：$\gamma$严格控制着B2相的析出、短程有序程度以及晶粒细化。此外，当γ值约为2.0（$Ti_{46}Al_{10.5}$合金）时，能实现高屈服强度（>1 GPa）和高拉伸延展性（>20%）的最佳协同效应，而γ值过高则会导致脆化。本研究确立γ为关键组成参数，并通过综合参数控制和元素比例控制为设计高性能轻质高熵合金提供了一个实用框架。

关键词：轻质高熵合金；经验参数；铝/钛比；B2相；短程有序；微观结构；力学性能

作者简介：罗峰林，男，2002年生，硕士，上海大学材料研究所，上海 200072，E-mail：lfl1015004291@shu.edu.cn